Long-wavelength undulations of the seismic Moho beneath the strongly stretched Western Anatolia

Hayrullah Karabulut, Anne Paul, Tugce Afacan Ergün, Denis Hatzfeld, Dean M Childs, Mustafa Aktar

Geophysical Journal International

Geophys. J. Int. (2013) **194,** 450–464
Advance Access publication 2013 April 4

doi: 10.1093/gji/ggt100

Long-wavelength undulations of the seismic Moho beneath the strongly stretched Western Anatolia

Hayrullah Karabulut,[1] Anne Paul,[2] Tugce Afacan Ergün,[1] Denis Hatzfeld,[2] Dean M. Childs[1] and Mustafa Aktar[1]

[1]*Boğaziçi University, Kandilli Observatory and Earthquake Research Institute,* 34684 *Çengelköy Istanbul, Turkey. E-mail: kara@boun.edu.tr*
[2]*Institut des Sciences de la Terre, Université Joseph Fourier Grenoble*-1*, CNRS, F*-38041 *Grenoble, France*

Accepted 2013 March 11. Received 2013 March 11; in original form 2012 October 4

SUMMARY

Western Turkey provides spectacular examples of the two end-member models of deformation of the continental lithosphere, with strain localization along the North Anatolian fault and distributed north–south extension along the Aegean coast. To provide constraints on the mechanisms of continental deformation, we present a new high-resolution image of lithospheric structure along a ∼650 km transect crossing Western Anatolia at 28°E longitude from the Black Sea to the Mediterranean. More than 2600 receiver functions are computed from records of teleseismic earthquakes at 40 broadband seismic stations with an average spacing of 15 km. Lateral variations of crustal thickness and *Vp*/*Vs* ratio are inferred from both *H*-*k* and common conversion point stacks. We observe long-wavelength variations of Moho depth from ∼31 km in the Thrace basin to ∼25 km beneath the Marmara Sea, ∼32 km beneath the Izmir–Ankara suture, ∼25 km beneath the Menderes Massif and ∼20 km on the coast of the Mediterranean. No mid- or lower-crustal interface is visible in the migrated depth section and seismic discontinuities are confined to the shallow crust. The small-amplitude and long-wavelength lateral variations of the Moho topography suggest that viscous flow in a hot lower crust has smoothed out the lateral variations of crustal thickness induced by Cenozoic continent–continent collision. The crust–mantle boundary is flat beneath the central and southern Menderes Massif. The rougher Moho topography and more heterogeneous crust of the Marmara region likely result from transtension in the North Anatolian Fault Zone superimposed onto Aegean extension. The Moho of the subducted African lithosphere is observed dipping northward between ∼40 and ∼60 km depth at the southern end of the profile. The abrupt termination of the subducted slab only 50 km to the north of the Mediterranean coast confirms the slab tear inferred from previous tomographic studies.

Key words: Composition of the continental crust; Seismicity and tectonics.

1 INTRODUCTION

The way continents deform and the rheology of the continental lithosphere or the forces driving deformation are still debated. A controversy on the rheology of the continental lithosphere initially arose on the example of Asian tectonics. According to the end-member model of Tapponnier *et al.* (1982), the continental lithosphere deforms as a set of rigid or elastic blocks separated by major strike-slip faults where most of the strain is localized. In contrast, England & McKenzie (1982) argued that continents deform like a viscous continuum. The relative strengths of the upper crust, lower crust and mantle lithosphere are also matters of debate (Jackson 2002; Watts & Burov 2003). Yet, the presence of decoupled layers is a key question to understand whether flow in the asthenospheric mantle and induced strain at the base of the lithospheric mantle can be transferred to the upper crust and control surface deformation.

Besides Asia, the rapidly deforming Aegean-Anatolian region has focused attention as it includes one of the best-documented examples of major continental strike-slip fault with clear strain localization, the North Anatolian Fault (NAF), together with a broad area of distributed deformation in the Aegean Sea and Western Anatolia (see review by Jolivet *et al.* 2012 and references therein). As the two end-member rheological models coexist, the debate is currently less focused on the rheology of the Aegean lithosphere than on the engine of deformation. While the collision of Arabia with Eurasia has long been considered as the only driving force of the westward motion of the Anatolian microplate (e.g. Dewey & Şengör 1979; Armijo *et al.* 1999), the role of the retreat of the Hellenic trench and the associated slab pull in the recent to present

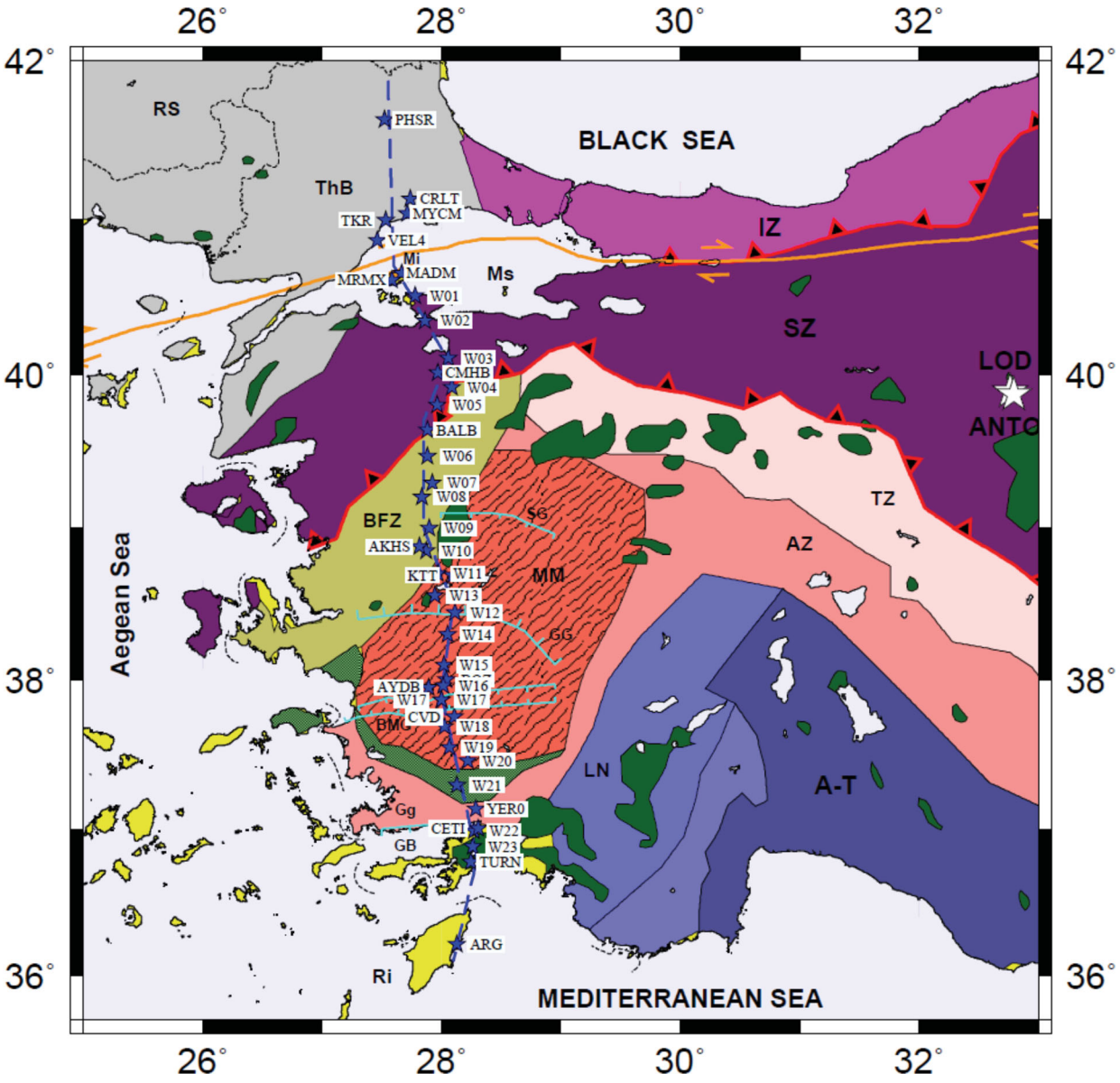

Figure 1. Map of permanent and temporary seismic stations deployed on the western linear transect of the SIMBAAD experiment (blue stars). The morpho-tectonic units and the major tectonic features of the region are also shown; ATB, Anatolide-Tauride Block; AZ, Afyon Zone; BFZ, Bornova Flysh Zone; BMG, Büyük Menderes Graben; GG, Gediz Graben; GB: Gökova Bay; Gg, Gökova Graben; SG, Simav Graben; GB, Gökova Bay; IZ, Istanbul Zone; LN, Lycian Nappes; MM, Menderes Massif; PT, Pontides; RS, Rhodope-Strandja Basin; SZ, Sakarya Zone; IASZ, Izmir–Ankara Suture Zone; Ms, Marmara Sea; Mi, Marmara Island; NAFZ, North Anatolian Fault Zone; Ri, Rhodos Island; ThB, Thrace Basin; TZ, Tavşanlı Zone. Red lines with black triangles show the sutures. The thin light blue lines show the major normal faults of the grabens and the magenta line shows the NAF. The dark green units represent the ophiolite outcrops. The migrated RF depth section was computed along the profile shown as a blue line. Geological map modified from Okay & Tüysüz (1999) and van Hinsbergen *et al.* (2010).

kinematics was highlighted by GPS velocity data (Reilinger *et al.* 2006). Moreover, recent models underline the additional parts played by body forces in the deformation of the upper crust of Anatolia (gravitational potential energy; Özeren & Holt 2010) and/or to forces applied at its base by the mantle (basal drag; Faccenna & Becker 2010) in the absence of strongly decoupling layers.

Western Turkey is a natural laboratory for continental deformation studies as it is experiencing both localized strike-slip deformation along the NAF, and Basin and Range type pervasive, roughly north–south continental extension (see review in Çemen 2010). Geological evidences of N-S extension are numerous in the Menderes Massif (Fig. 1). It is crosscut by the high-angle normal faults of the still-active east-trending Gediz and Büyük Menderes grabens. Moreover, it is one of the largest metamorphic core complexes which are domes of deep crustal rocks exhumed and deformed during continental extension (Lister *et al.* 1984; Gessner *et al.* 2001; Tirel *et al.* 2008). As such, the Menderes Massif has been considered as the eastern continuation of the Cycladic Massif of the Aegean (Bozkurt & Oberhänsli 2001). The extensional exhumation of metamorphic rocks in the Menderes Massif accompanied orogenic collapse of the crust previously over-thickened by the collision between the Anatolide-Tauride block and the Sakarya microcontinent along the Izmir–Ankara suture (Şengör & Yılmaz 1981; Bozkurt & Oberhänsli 2001; Fig. 1). Extensional deformation

and core-complex formation started in the Early Miocene. The age of the grabens is more controversial and ranges from Miocene to Pliocene (Bozkurt & Oberhänsli 2001 and references therein). In Northern Anatolia, motion along the shear zone that was to become the NAF started in the Late Mid-Miocene, after the initiation of north–south extension (Le Pichon *et al.* 2001). Thereafter, the extrusion of Anatolia might have played a part in its late phases, but extension most probably originated from the combination of gravity collapse of an over-thickened orogenic crust (Gautier *et al.* 1999) and backarc spreading due to the retreat of the Hellenic trench (Le Pichon & Angelier 1979, 1981; Lister *et al.* 1984; Brun & Faccenna 2008). The retreat is attested by the distribution and ages of magmatic rocks in the Aegean Sea which document a regular migration of the magmatic arc from 35–30 Ma to the present (Pe-Piper & Piper 2006; Jolivet *et al.* 2009). Moreover, an intense Miocene magmatic activity in Western Anatolia is interpreted by de Boorder *et al.* (1998) as evidence for a slab tearing episode which might have accelerated southwestward retreat of the eastern edge of the Hellenic slab and strengthened extension in Western Anatolia. Then, the retreat of the Hellenic trench may have favoured the westward escape of Anatolia from the Arabian collision zone and the initiation of shear along the future NAF (e.g. Le Pichon & Kreemer 2010, and references therein).

In complement to petrology and structural geology, satellite geodesy and seismotectonic studies provide decisive data on the debate of processes of continental deformation in Western Anatolia. While Turkey was considered as one of the best examples of the rigid block model of continental deformation by McClusky *et al.* (2000), the very dense GPS data set of Aktuğ *et al.* (2009) has lead to a very different model of Western Anatolia deforming as a continuum. Aktuğ *et al.* (2009) show that integrated north–south extension at 27° longitude exceeds 20 mm yr^{-1}, close to the 20–25 mm yr^{-1} of right lateral shear measured along the NAF. As such, Western Anatolia is one of the most rapidly extending continental regions. McClusky *et al.* (2000) and Reilinger *et al.* (2006) observed a strain rate of 400–600 nstrain yr^{-1} concentrated within a few tens of kilometers around the NAF. Further south, between the Aegean coast and 31.5°E longitude, significant extensional rates of 40–60 nstrain yr^{-1} are measured almost everywhere by Aktuğ *et al.* (2009) except in the Büyük Menderes and Gediz grabens where north–south extension reaches 140 and 85 nstrain yr^{-1}, respectively. The geodetic data are confirmed by the observation of diffuse seismicity and spatially very coherent focal mechanisms with T-axes oriented NNE-SSW (Kiratzi & Louvari 2003).

The flat and continuous Moho imaged in the Basin and Range extensional province of Western U.S.A. by seismic reflection profiles was interpreted as a young feature related to Cenozoic extension (Klemperer *et al.* 1986; Hauser *et al.* 1987), where topography had been wiped out by ductile crustal flow at the regional scale (e.g. Block & Royden 1990). Since then, a flat Moho is considered as the signature of stretched continental crust and it has become a key constraint in models of metamorphic core complexes (e.g. Tirel *et al.* 2008). In Western Anatolia, the Moho topography has never been investigated at large scale and high resolution. The first high-resolution image of the crustal structure in the extended province was provided by a receiver function (RF) profile along a 100-km-long profile confined in the central Menderes Massif in-between the Gediz and Büyük Menderes grabens (Zhu *et al.* 2006). It displayed a flat Moho at 26–28 km depth, 4–8 km above the Moho imaged at isolated seismic stations in the eastern part of the Menderes Massif (KUL: 30 km) or in the central Anatolian plateau (ANTO: 36 km). Zhu *et al.* (2006), however, concluded that their profile was too short to determine the shape of the Moho depth change across the boundaries of the core complex. Other estimates of the crustal thickness in Western Anatolia rely on sparse distributions of permanent seismic stations (Saunders *et al.* 1998; Sodoudi *et al.* 2006). The regional variations of the crustal thickness were also inferred from the estimates of surface wave group velocities (Cambaz & Karabulut 2010; Hubans 2010) and *Pn* tomography (Mutlu & Karabulut 2011); but the spatial resolution of these studies is larger than 100 km. The most detailed image of the crustal structure in Western Turkey is provided by the multi-method onshore–offshore seismic probing of the northern Marmara basins by Bécel *et al.* (2009). They identify the Moho at 26 km depth beneath the Northern Marmara Trough; it steps down abruptly by 5 km beneath the eastern and western rims of the Sea of Marmara; but the north–south crustal thickening is smoother and more subtle as a depth change of 2 km is measured beneath the southern margin of the Sea of Marmara, 30 km to the south of the North Marmara Trough.

From the inversion of gravity data in the Aegean Sea, Tirel *et al.* (2004) inferred a flat Moho and thin crust (25 km) beneath the Cycladic metamorphic core complex, which might be the western counterpart of the Menderes Massif. Due to the difference in elevation, Western Anatolia is, however, believed to have a thicker crust than the Aegean Sea.

In this study, we probe the crustal structure of Western Anatolia along a north–south section at 28°E longitude from the Black Sea coast to the Mediterranean coast (Fig. 1). In order to give clues on crustal thickness variations associated with continental extension, the almost linear profile crosses the NAF, the basins of the Marmara Sea, the Menderes Massif and its core complexes and grabens. We use seismic records of a dense (15 km spacing) temporary array installed for 1 yr in the framework of the seismic imaging of the mantle beneath the Aegean-Anatolia domain (SIMBAAD) project (Salaün *et al.* 2012). The RF technique is used to determine crustal thickness and *Vp*/*Vs* ratio which provides reliable indications on the felsic or mafic character of crustal rocks. We show that Western Anatolia has a thin crust, but not a flat Moho as beneath the Basin and Range.

2 DATA AND PROCESSING

In the spring of 2007, as part of the SIMBAAD project, we installed a temporary array of 33 broadband seismic stations in Central and Western Turkey, Greece and Southern Bulgaria for 2 yr duration. The array filled the gaps in the permanent broadband networks (∼90 stations) providing an inter-station spacing of ∼100 km across the region (Salaün *et al.* 2012). The experiment also included two north–south linear profiles of 1 yr duration with more densely spaced broadband stations.

This paper focuses on the first profile installed in Western Turkey along the coast of the Aegean Sea crossing major structures almost perpendicularly to their east–west strike (Fig. 1). A total of 23 stations were deployed from the Marmara Island in the north to the Gökova Gulf in the south. The extension of the line to Rhodos Island in the south and Thrace in the north with the use of permanent stations increased the length of the profile to ∼650 km. Broadband data from the previous experiment described by Zhu *et al.* (2006) and permanent networks increased to 40 the number of stations on the profile with an average inter-station distance of 15 km (see Table 1).

The array crosscuts several continental fragments that were accreted by the Early Cenozoic closure of the Tethys Ocean and

Table 1. Station coordinates and parameters of Earth structure used to compute migrated images.

No	Name	Lat (°)	Lon (°)	Elev (m)	*H* (km)	*Vp*/*Vs*	*Vp* (km s^{-1})	*Vpn* (km s^{-1})
1	PHSR	41.630	27.524	262	30.5	1.75	6.2	8.2
2	CRLT	41.128	27.736	217	29.0	2.20	6.2	8.2
3	TKR	40.989	27.535	148	26.0	1.85	6.2	8.2
4	VEL4	40.863	27.459	−900	25.5	1.90	6.2	8.1
5	MRMX	40.609	27.583	687	25.0	2.00	6.2	8.1
6	W01	40.506	27.777	27	25.5	1.95	6.2	8.1
7	W02	40.346	27.862	246	25.5	1.90	6.2	8.0
8	W03	40.108	28.058	112	28.5	1.85	6.2	8.0
9	GONE	40.047	27.686	150	28.5	1.85	6.2	8.0
10	CMHB	40.012	27.970	212	28.5	1.85	6.2	8.0
11	W04	39.918	28.086	397	28.5	1.82	6.2	8.0
12	W05	39.803	27.963	447	30.0	1.82	6.2	8.0
13	BALB	39.640	27.880	159	31.0	1.83	6.2	8.0
14	W06	39.468	27.884	201	31.0	1.66	6.2	8.0
15	W07	39.296	27.921	548	31.5	1.66	6.2	8.0
16	W08	39.204	27.834	277	31.5	1.66	6.2	7.9
17	W09	38.998	27.895	417	31.0	1.75	6.2	7.9
18	AKHS	38.879	27.814	217	30.5	1.75	6.2	8.9
19	W10	38.849	27.874	104	30.5	1.75	6.2	8.0
20	W11	38.703	27.969	91	30.0	1.75	6.2	8.0
21	KTT	38.688	28.093	100	29.5	1.75	6.2	8.0
22	W13	38.559	27.942	72	28.0	1.75	6.2	8.0
23	W12	38.446	28.112	305	27.5	1.75	6.2	8.0
24	W14	38.301	28.049	1198	27.5	1.80	6.1	8.0
25	W15	38.098	28.021	270	25.5	1.80	6.1	8.0
26	BOZ	38.000	28.040	1240	25.5	1.80	6.0	8.0
27	W16	37.960	28.017	670	25.5	1.80	6.0	8.0
28	AYDB	37.946	27.89	1202	25.0	1.80	6.0	8.0
29	W17	37.864	27.999	71	25.0	1.80	6.0	8.0
30	CVD	37.752	28.107	71	25.0	1.82	6.0	8.0
31	W18	37.687	28.027	217	25.0	1.85	6.0	8.0
32	W19	37.549	28.065	88	24.0	1.85	6.0	8.1
33	W20	37.458	28.219	446	24.0	1.85	6.0	8.1
34	W21	37.293	28.128	433	24.0	1.95	5.9	8.0
35	YER0	37.136	28.286	665	23.0	2.25	5.9	8.0
36	CETI	37.003	28.307	45	23.0	1.85	5.9	8.0
37	W22	36.984	28.271	27	23.0	1.85	5.9	8.0
38	W23	36.877	28.262	123	23.0	1.85	5.9	8.0
39	TURN	36.775	28.244	150	23.0	1.85	5.9	7.9
40	ARG	36.216	28.126	181	19.0	1.85	5.9	8.2

consequent continent–continent collisions (Okay & Tüysüz 1999). In the north, the Istanbul Zone (IZ in Fig. 1) and the Sakarya Zone (SZ) form the Pontides belt along the Early Eocene Intra-Pontide Suture (IPS). The NAF follows the course of the older Intra-Pontide Suture in the Sea of Marmara. Further south, the Late Paleocene accretion of the Anatolide-Tauride Block to the Sakarya microcontinent along the Izmir–Ankara Suture (IAS) has led to the superposition of different units separated by major thrusts to the north of the Menderes Massif (MM). They are from north to south: the blueschists and ophiolites of the Tavşanlı zone (TZ), the Bornova flysch zone (BFZ) and the blueschist metamorphosed sediments of the Afyon zone (AZ). According to Okay & Tüysüz (1999), the two separate oceanic lithospheres of Paleo-Tethys and Neo-Tethys have been consumed along the Izmir–Ankara Suture leading to a major orogen and significant crustal thickening. As outlined in the introduction, subsequent orogenic collapse and backarc spreading induced continental extension and the Early Miocene exhumation of the Menderes metamorphic core complex.

To the south, the African plate is subducting beneath the Aegean with a relative velocity of 4 cm per year. Shallow seismicity around Rhodos Island has an apparent dip of 35° to the north and disappears at a depth of ∼55 km. An EW-striking zone of micro-seismicity is observed in the Gökova Gulf reaching a depth of 20 km.

The 1-yr deployment recorded more than 100 events with magnitudes ≥5.5 at teleseismic distances between 30° and 95° and 60 events were selected with fair signal-to-noise ratio (Fig. 2). The azimuthal coverage is non-uniform as a majority of events come from the Western Pacific subduction zones and few from the Atlantic and Indian Oceans. Data from the permanent stations on the profile for time periods longer than the temporary deployment were also included in the analysis.

2.1 Computation of RFs

The RF method is now routinely used to determine crustal and upper mantle structures from three-component seismic data (Langston 1977; Owens *et al.* 1984). Rotation of three-component recordings of distant earthquakes into the local Z-R-T ray-based coordinate system isolates the *P* to *S* converted phases on the radial component. The deconvolution of the vertical component from the radial removes the earthquake source signature and travel path effects from

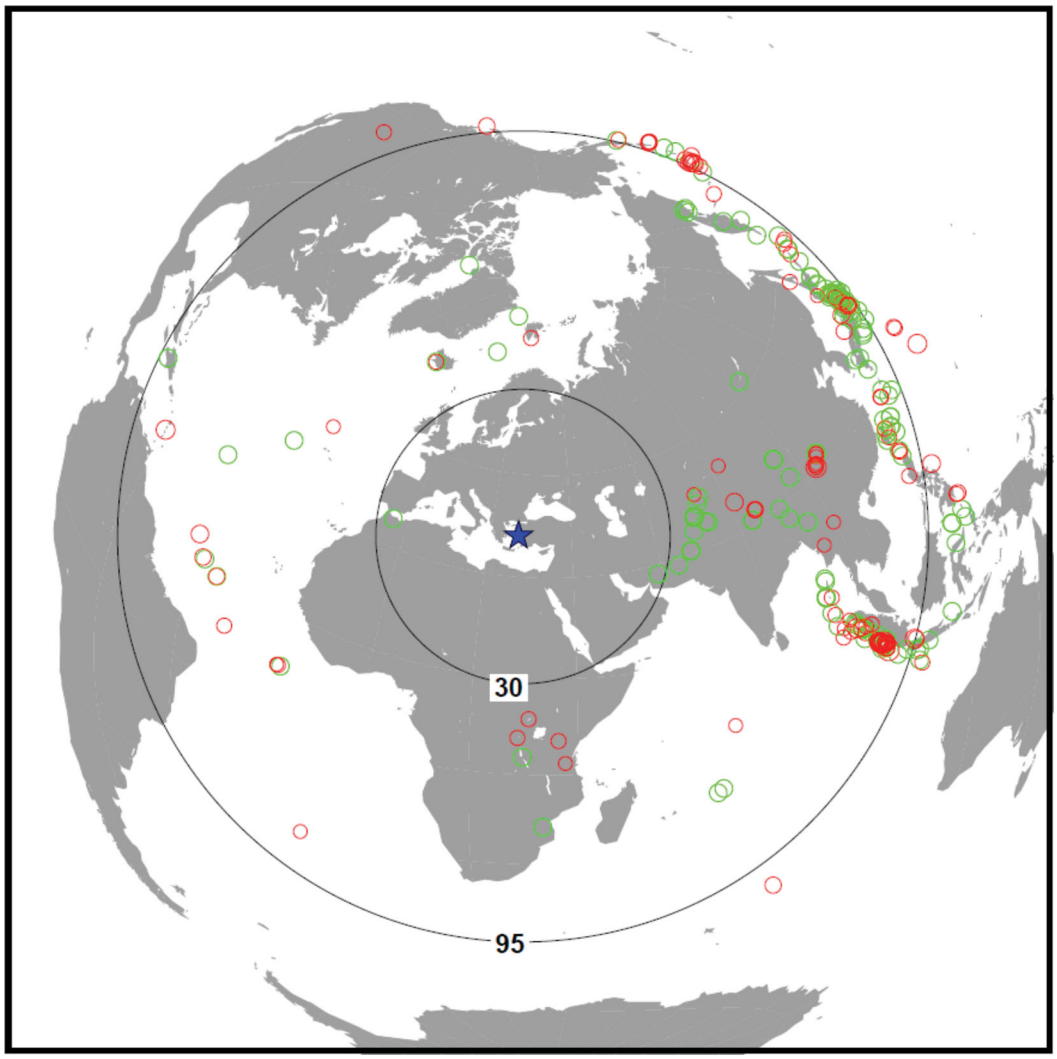

Figure 2. Equidistant projection of the locations of teleseismic events used in this study (red: recorded by temporary stations, green: recorded by permanent stations). The two circles represent epicentral distances of 30° and 95°.

the source to beneath the recording station. The final radial RF contains, in addition to the primary converted phases, multiple phases generated by reflections between the Earth's surface and velocity discontinuities. The time delay between converted *S* and direct *P* waves is proportional to the depth of the converting interface and the average velocity structure above it. Including the multiples in the RF analysis provides additional information on the depth of the discontinuity and the average Poisson's ratio above it (Zandt & Ammon 1995; Zhu & Kanamori 2000).

We computed radial and transverse RFs using the time-domain iterative deconvolution method of Ligorria & Ammon (1999). The time series were convolved with a Gaussian function for alpha parameter 5.5. The RFs were visually inspected by sorting them according to back azimuth and distance. Radial and transverse RFs with anomalous shapes and amplitudes were discarded. At the end, we obtained more than 2600 RFs along the profile.

We also computed RFs with common source time function for each event (Tseng & Chen 2006). The waveforms from each teleseismic event were aligned on the first *P* arrival time using cross correlation with a reference station of high signal-to-noise ratio (S/N). Then, the vertical components of an event with similar instruments along the profile were stacked to obtain source time functions. Two different source time functions for each event representing each halves of the profile were estimated. Both methods provided consistent results when the S/N is high. However, deconvolution with common source time functions provided higher quality RFs when the S/N was low for the vertical component. We therefore combined both approaches to estimate RFs at each station.

2.2 Common conversion point migration

To produce a depth image of the lithosphere and upper mantle beneath the linear receiver array, we performed a common conversion point (CCP) depth migration of the *P*-to-*S* converted phases (thereafter referred to as *Ps*) using the method described by Zhu (2000). A modified IASP91 standard Earth model with variable *P*-wave velocity and *Vp*/*Vs* beneath each station was constructed along the profile. The 2-D model space was subdivided into a two-dimensional grid of cells. The RFs were back-projected from the receiver to the source through these cells with constant ray parameters. The amplitude of each cell was obtained by averaging amplitudes of the radial RF of the crossing ray paths.

The initial estimate of crustal thickness (H) and Vp/Vs (k) was obtained from a grid-search stacking of the *Ps* phase and the multiples, *PpPs* and *PsPs+PpSs* (Zhu & Kanamori 2000). This analysis assumes that the incoming plane *P* wave is sampling the structure beneath the receiver composed of locally flat homogeneous layers. The RFs at each station are stacked using unequal weights (0.7, 0.2 and 0.1) for the three converted phases. The amplitude of stacked traces is maximized where the three multiples add constructively. The success of the technique relies on a good azimuthal coverage of events and the existence of multiply reflected energy (see Fig. S1).

Figs 3(a) and (b) show results of *H-k* analysis at permanent station BALB located within the Sakarya Zone. It has a fairly good S/N compared to other stations on the profile. The Moho multiples can be observed clearly in Fig. 3(a) with a sharp Moho conversion at ∼4 s. The crustal thickness and Vp/Vs are estimated as 32 km and 1.81, respectively (Fig. 3b). This analysis was performed on all stations of the profile and the results are presented in Table 1. The variances of H and k can be calculated from the width of the energy spot in the *H-k* plane. Large uncertainties are due to the absence of multiple energy or the violation of the hypothesis of a locally flat, homogeneous Earth structure beneath the station.

To improve the CCP migration, which requests knowledge or assumption on the crustal *P*-wave velocity, we computed average crustal *P*-wave velocities from local earthquakes with epicentres located within 10 km of the profile. A total of 20 earthquakes with magnitudes $3 < \mathrm{Ml} < 4$ were selected for this analysis. The earthquakes were located and the average crustal *P*-wave velocities were computed from travel time–distance curves (see Fig. S2). The obtained average crustal *P*-wave velocities used to compute the CCP depth sections are given in Table 1. At permanent stations with long recording time, we also computed *Vp* and *Vs* from earthquakes concentrated in their vicinity to compare with *H-k* analysis. At station BALB, the estimates of Vp/Vs from travel–time curves and *H-k* method are in reasonable agreement (Fig. 3c).

Table 1 shows that Vp/Vs undergoes rapid and large variations beneath the profile, while *Vp* varies smoothly. As there might be a trade-off between crustal thickness and Vp/Vs in the *H-k* analysis, we furthermore tested the accuracy of our estimates by computing CCP images of the *PpPs* and *PpSs* multiples which are more sensitive to Vp/Vs than the primary *Ps* (Hetenyi 2007). If the images obtained from the multiples display a converted phase at the same depth as the Moho image in the *Ps* migrated section, the estimates of crustal thicknesses and Vp/Vs values are reliable (Fig. 4). When the converted phases do not coincide, the depth differences can be used to adjust the value of the crustal Vp/Vs.

The horizontal resolution of the CCP migrated image is determined by the Fresnel zone of the incident *P* wave which broadens with depth. The vertical resolution depends on seismic discontinuities being separated by more than 1/4 of the *S*-wave wavelength (Zhu *et al.* 2006). In this study, the vertical resolution is in the range 3.5–4 km and the radius of the corresponding Fresnel zone is approximately 10 km at 30 km depth. Using a migration mesh of 3 km in the horizontal direction and 0.5 km in the vertical direction, we therefore adopted a smoothing window of 15 km horizontally and 2 km vertically. We also computed CCP images for three ranges of back-azimuth (30°–150°, 150°–270° and 270°–30°) to detect possible dependency of the images on the locations of earthquakes. The uncertainties on the Moho depth are estimated from the migrated RF depth sections. However, the true uncertainty also results from uncertainties on Vp/Vs and *Vp*. A 3 per cent uncertainty on Vp/Vs results in a 2 km error on the Moho depth, while the same uncertainty on *Vp* results in a 1 km error (Zhu *et al.* 2006).

3 RESULTS

Fig. 5 shows the results of CCP analysis. The top panel (Fig. 5a) shows the topography and Bouguer gravity anomaly along the profile (Ateş *et al.* 1999). The gravity values are high in the northern part of the profile reaching 50 Mgal in the Marmara Sea. The second panel (Fig. 5b) indicates locations of the major structural boundaries along the profile. Figs 5(c) and (d) show the CCP time-to-depth migrated section, with no vertical exaggeration (Fig. 5c) and a vertical exaggeration of 2 (Fig. 5d). The migration takes into account lateral variations of Vp/Vs estimated from *H-k* stacking and updated with the results of CCP stacking of multiples. Positive amplitudes (red) are generated by a velocity increase with depth, whereas negative amplitudes (blue) correspond to a velocity decrease. Hypocenters of local earthquakes located within a band of 20 km along the profile are superimposed on the CCP section in Fig. 5(d). The bold black line is the conversion on the Moho. A ±2 km uncertainty is estimated on the Moho picks from the migrated RF depth sections.

To quantify the effectiveness of the Moho in producing wave conversions, we computed the *R*-factor shown in Fig. 5(e) as the stacked amplitude of the *Ps* and multiple phases normalized by the amplitude of the direct *P* as suggested by Nair *et al.* (2006). The amplitude of the converted Moho phases depends on the velocity contrast between crust and mantle, the thickness of the Moho transition zone and the short-scale topography of the Moho. A sharp Moho with strong velocity contrast produces *Ps* and multiples with strong amplitudes, leading to a high value of R (Nair *et al.* 2006). The regional average of R is 0.25, while the largest values (∼0.45) are observed beneath the southern Menderes Massif (Fig. 5e).

Fig. 5(f) shows the final estimates of crustal thickness (black curve) and Vp/Vs (red curve) from the CCP images which may differ from the initial estimates of the *H-k* stack given in Table 1. The Vp/Vs ratio provides useful information on the composition of the continental crust. High values tend to correspond to rocks of more Mafic composition, while low values are associated with rocks that contain large amounts of quartz (Fountain & Christensen 1989). The presence of fluids or partial melt reduces shear wave velocities more than compressional wave velocities resulting in high Vp/Vs values. The crustal average Vp/Vs ratio measured along the array ranges from 1.65 to 2.0 (red curve in Fig. 5f) with an average of 1.78, slightly above the global average of continental crust (Christensen 1996).

We also display in Fig. 5g Love wave group velocities at 20 s (Cambaz & Karabulut 2010) and *Pn* velocities along the profile (Mutlu & Karabulut 2011).

Overall, the Moho is observed as a laterally continuous strip of positive amplitude between 25 and 32 km depth (Figs 5c and d). The *PpPs* multiple appears with laterally discontinuous positive amplitudes in the 90–120 km depth range in Fig. 5(c). Beneath the Thrace Basin, the Moho depth is ∼29 km and the thick sedimentary basin of ∼9 km (Görür & Okay 1996) induces strong multiples which alter the migrated image to large depths. The crustal thickness decreases to 25 km beneath the Marmara Sea. The transition from the Marmara Sea to the Sakarya Zone displays a gradual thickening of the crust from 25 to 30 km. In the Sakarya Zone, the crustal thickness increases to a maximum of 32 km beneath the Izmir–Ankara Suture. From the Sakarya Zone to the Lycian nappes in the south, the crust–mantle boundary is clearly defined by a strong *Ps* and strong multiples, giving R values larger than 0.2. Again, the Moho depth decreases smoothly from its largest value of ∼32 km beneath the Izmir–Ankara Suture to ∼28 km beneath the Menderes

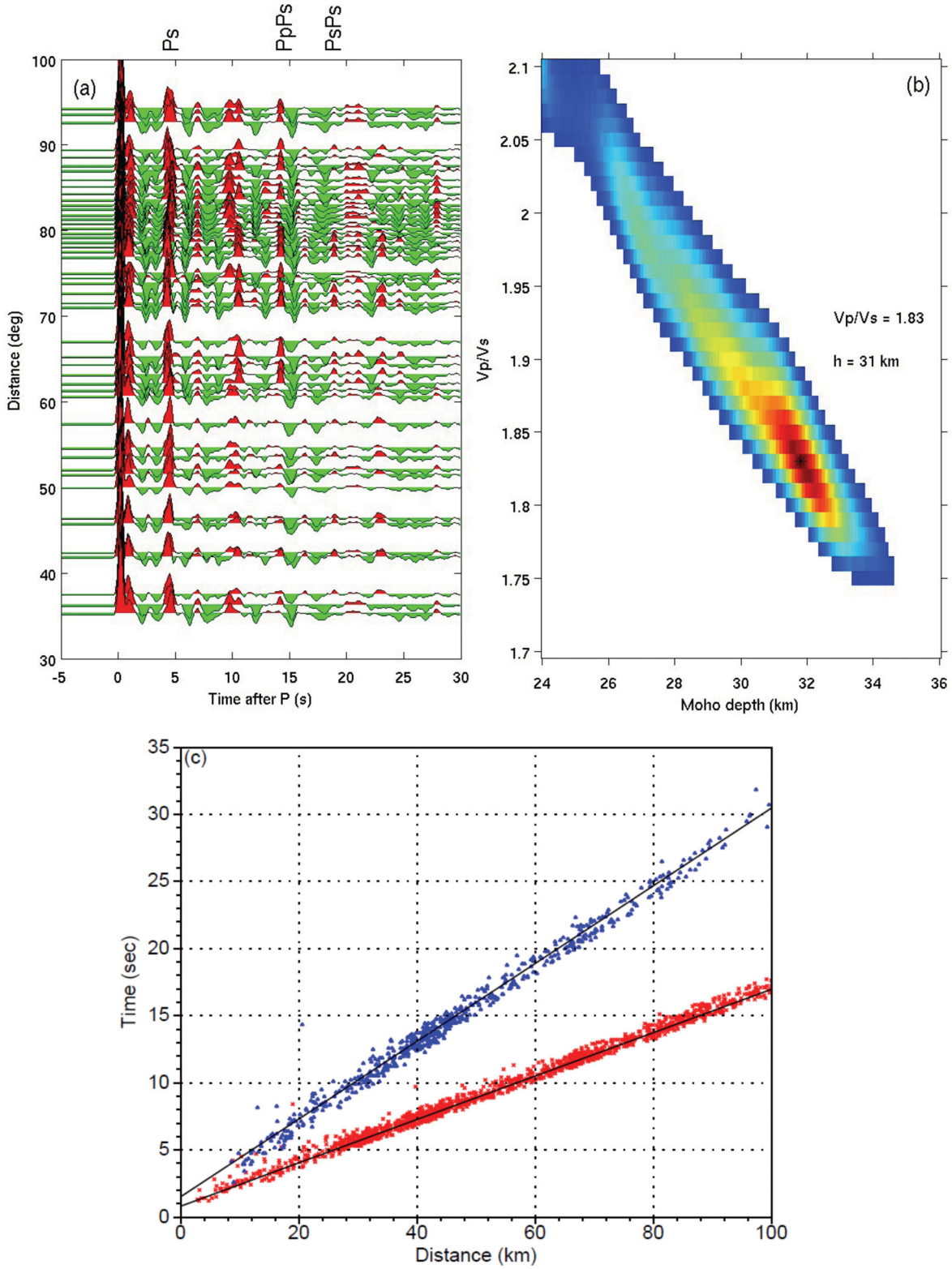

Figure 3. (a) RFs at station BALB sorted by epicentral distance. Traces in every 0.4° are displayed. (b) *H-k* stack of the RFs with estimated *Vp*/*Vs* and crustal thickness. (c) Travel time observations of local earthquakes recorded at station BALB. The average crustal *Vp* and *Vs* values are estimated from the slope of the related travel time curves (blue dotted line: $Vp = 6.2$ km/s, red dotted line: $Vs = 3.5$ km/s).

Massif (Fig. 5f). The Moho below the Menderes is relatively flat and continuous, as shown for its central part by Zhu *et al.* (2006). It is characterized by *Ps* and *PpPs* phases of very strong amplitudes as shown by the CCP section of Fig. 5(c) (*PpPs* multiple in the 90–120 km depth range) and the highest values of *R* (Fig. 5e). Further south beneath the Lycian Nappes, we observe changes both in the character of the reflectivity and the Moho depth. The amplitude of the converted phase weakens abruptly at stations of the

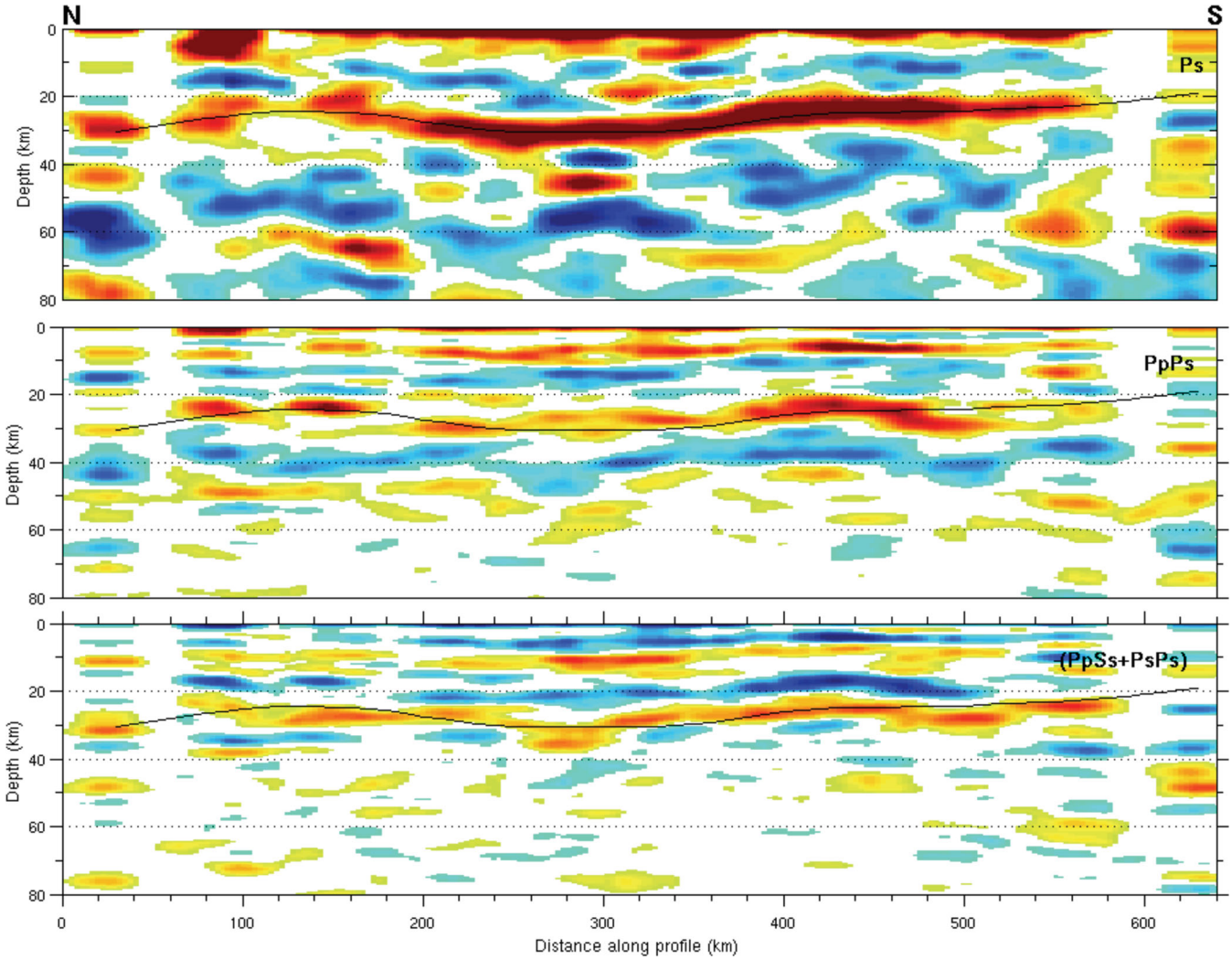

Figure 4. Migrated depth sections of Ps (a), PpPs (b) and PpSs+PsPs (c) modes (note that the sign of and PpSs+PsPs section is reversed). The black line shows the crust–mantle boundary as in Fig. 5(c). The Moho depth estimates in the three sections should be similar if the velocity model used in the migration is accurate. We used larger smoothing parameters in both vertical and horizontal directions as the PpPs and PpSs+PsPs contain strongly scattered multiple energy. The three images show consistent results beneath the Sakarya Zone and Menderes Massif, while differences are observed beneath the Marmara Sea and the Aegean. As a whole, the strong similarities between the three migrated sections indicate that the *Vp*/*Vs* model is accurate and the depth section of Fig. 5 is reliable.

Mediterranean coast. We, however, image a thin crust (∼20 km) beneath the Rhodos Island at the southern end of the profile.

4 DISCUSSION

4.1 A thin crust with long-wavelength Moho undulations

As expected for an extensional continental domain, the average crustal thickness measured along the profile is low: 27 km. Our high-resolution observations on a profile spanning the whole width of Western Turkey thus confirm the sparser observations of Saunders *et al.* (1998), Zhu *et al.* (2006), Bécel *et al.* (2009) or the lower resolution Moho map of Mutlu & Karabulut (2011). More precisely, our estimates of Moho depth are 1 to 5 km smaller than the measurements of Zhu *et al.* (2006) conducted at the same locations (BALB, BOZ, central Menderes) using the same RF analysis. The discrepancy is explained by our estimated higher values of the average crustal *Vp*/*Vs*. Zhu *et al.* (2006) could estimate *Vp*/*Vs* at only a few broadband stations and they had to assume a constant *Vp*/*Vs* of 1.76 for the CCP migration of their profile in the Central Menderes Massif where we find 1.81 (Table 1). Our estimates are probably more reliable than those of Zhu *et al.* (2006) because our array is only composed of broadband stations with many years of recordings at the permanent stations. We checked the results of the *H-k* stack by migrating the multiples (Fig. 4). Similarly, Sodoudi *et al.* (2006) estimated a crustal thickness of 25 km beneath Rhodos Island (station RODO) assuming that *Vp*/*Vs* is 1.73 while we find 19 km at station ARG with measured *Vp*/*Vs* of 1.85. Bécel *et al.* (2009) estimated a crustal thickness of 26 km in the Northern Marmara Trough from offshore–onshore refraction and marine reflection profiles, very close to the 25 km that we measure at station MRMX.

The minimum 25-km thickness observed beneath the Sea of Marmara and the Menderes Massif is similar to the average crustal thickness measured in the Aegean Sea by reflection seismic (Makris 1978) or inversion of gravity data (Tirel *et al.* 2004). The average crustal thickness along our profile, 27 km, is slightly larger than

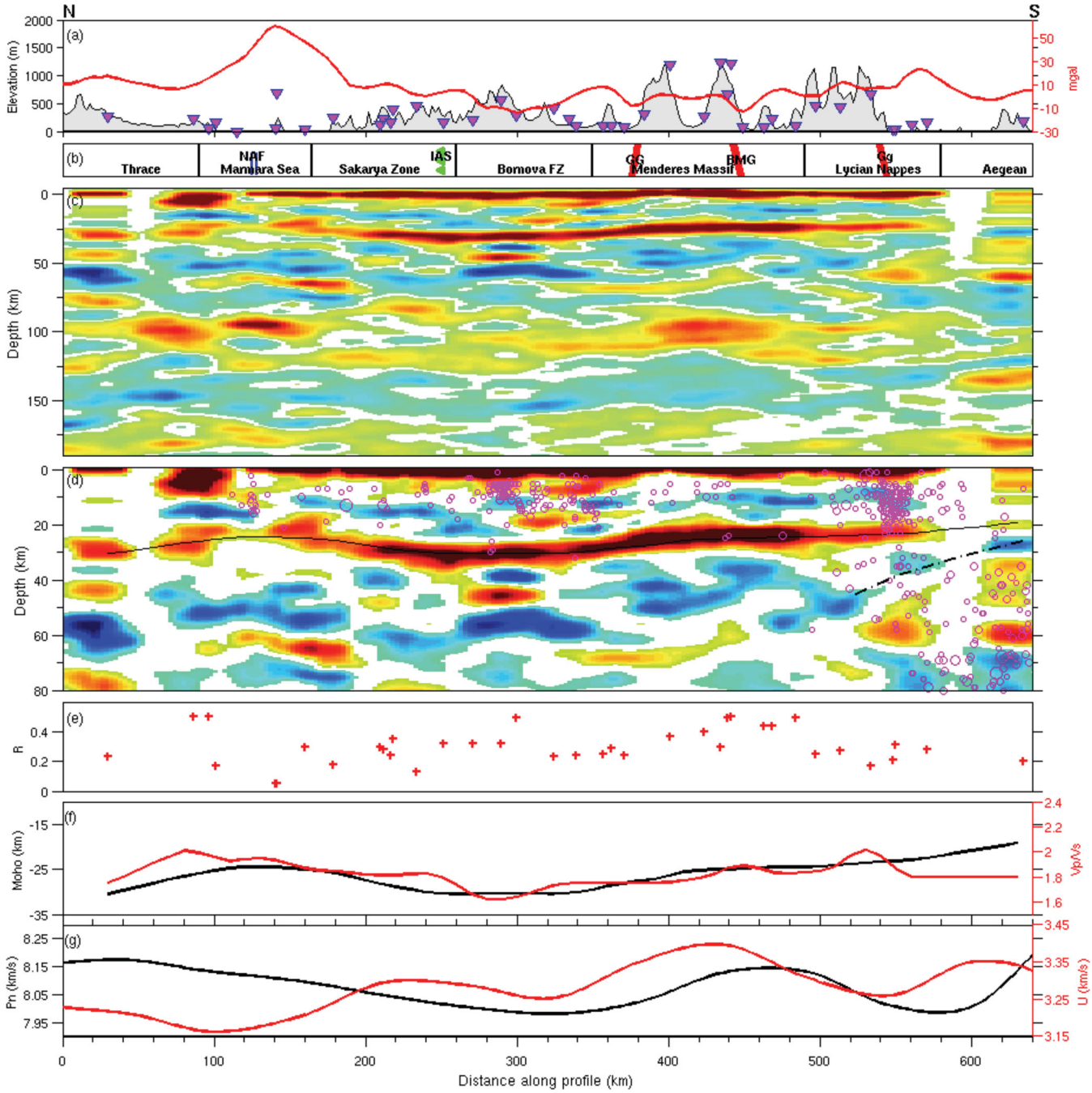

Figure 5. Migrated depth section of radial RF records of the Western Anatolia profile. Distance is measured with respect to the northernmost station. (a) Topography profile (black), receiver locations (magenta) and Bouguer gravity anomaly (red). (b) Geological units along the profile. (c) Common-conversion point depth migrated cross section (no vertical exaggeration). Red represents positive P-to-S converted amplitudes and indicates sharp increase in velocity with depth. The Moho is the continuous band between 26 and 32 km depth. (d) Common-conversion point depth migrated cross section with seismicity and major interpreted structures (vertical exaggeration 2). The seismic activity covers a period from 1998 to 2010 with magnitudes $M_l > 3.0$. (e) Ratio R of stacking amplitudes for each station. (f) Crustal thickness (black) and Vp/Vs (red) variations. (g) 20 s Love wave group velocities (red) and Pn velocities (black). Same abbreviations as in Fig. 1.

the average crustal thickness of 25 km estimated for the Aegean Sea by Tirel *et al.* (2004). This 2-km difference is not sufficient to explain the ∼700 m difference in elevation assuming isostatic compensation in the crust and average densities of 2700 kg m^{-3} for the crust and 3300 kg m^{-3} for the upper mantle. The 250-m residual elevation difference could be explained by dynamic topography defined as the dynamic response to convection in the underlying mantle (Gurnis 1990) and/or by isostatic compensation of lateral density contrasts within the mantle lithosphere. We do not favour dynamic topography as the main source of the elevation because it is a much smoother and broader scale effect. An isostatic uplift of Western Anatolia could be induced by a less dense and warmer upper mantle, while a downward pull of the Aegean Sea could be due to the dense and cold Hellenic slab. The static uplift of Western Anatolia does, however, not seem supported by seismic tomography of the upper mantle, as similar low-velocity anomalies are present

not only in the uppermost mantle beneath Western Anatolia but also beneath the Northern Aegean Sea (e.g. Salaün *et al.* 2012). To explain the residual topography difference between Western Anatolia and the Aegean Sea, we rather favour a localized downward pull of the Aegean by the Hellenic slab.

Fig. 5 documents the smooth topography of the Moho, with a maximum depth change of 6–7 km in 150 km distance from the Sea of Marmara (25 km) or the Menderes Massif (25 km) to the Bornova Flysh Zone (31.5 km). No sharp Moho depth change is imaged beneath the grabens of the Menderes Massif where the geodetic extension rate is much stronger than in the surroundings (Aktuğ *et al.* 2009), or beneath the deep pull-apart basins of the Sea of Marmara, although our station coverage is not sufficient there to detect Moho depth changes at spatial scale shorter than 20–30 km. Moreover, the Moho is flat (within 2 km) beneath the Central and Southern Menderes Massif. This observation is not surprising as such a flat Moho at regional scale is typically observed in regions of continental extension like the Basin and Range (Klemperer *et al.* 1986; Hauser *et al.* 1987) or the Aegean Sea (Tirel *et al.* 2004). The favoured mechanism for such a relaxation of Moho topography produced by differential shortening or extension is viscous flow in the lower crust weakened by high temperatures at Moho depth (e.g. McKenzie *et al.* 2000). The high temperatures may result from previous crustal thickening by continent–continent collision and consequent thermal relaxation and/or heating from below due to mantle delamination or asthenospheric rise in a slab window. All these processes might have contributed to the weakening of the lower crust of Western Turkey (e.g. Gautier *et al.* 1999; Wortel & Spakman 2000; van Hinsbergen *et al.* 2010; Salaün *et al.* 2012).

The Moho beneath Western Turkey is, however, not as flat as beneath the Basin and Range, as lateral Moho depth differences of 6–8 km are observed along the profile. If, like Zhu *et al.* (2006) and Aktuğ *et al.* (2009), we assume that the crustal thickness in the presently undeforming plateau of Central Anatolia is representative of the crustal thickness before extension started in Western Anatolia, we can estimate the spatial variations of the finite mean stretching factor β. With a crustal thickness of 37 km measured at station LOD in the Anatolian plateau (see location in Fig 1 and Fig S1), we find that β is 1.5 in the Sea of Marmara, 1.2 in the Bornova Flysch Zone, 1.5 in the Menderes Massif and 1.9 in Rhodos Island. From a comparison of the instantaneous strain rate and crustal thickness along an E-W profile from the Aegean coast to the central Anatolian plateau, Aktuğ *et al.* (2009) concluded that the distribution of crustal thickness in Western Turkey reflects the extension of a region of initially constant crustal thickness (37.5 km) at the present-day strain rate applied during the last 5 Ma. We confirm this observation on our N-S profile, where the variations of the β factor are qualitatively correlated with the instantaneous north–south extension rate measured from GPS by Aktuğ *et al.* (2009) and Floyd *et al.* (2010).

Crustal thickness variations in the same range have been inferred in the Aegean Sea from the inversion of gravity data by Tirel *et al.* (2004) who proposed to explain the Moho depth change by a two-stage extension. An Oligocene to mid-Miocene generalized gravitational collapse would have thinned the over-thickened crust of the Hellenides to a homogeneous thickness of 25 km in a Basin and Range type spreading of a weak and hot crust. Then, from the Mid-Miocene onwards, the extrusion of Anatolia would have amplified the extension by transtension in the North Aegean Trough leading to Moho depths smaller than 24 km, while the retreat of the Hellenic slab would have induced localized stretching in the Cretan Sea to a crustal thickness of 22–23 km, leaving the crust of the Cyclades almost unaffected. From modelling of a new detailed set of geodetic velocities for the Aegean and mainland Greece, Floyd *et al.* (2010) confirmed the suggestion made by a number of authors (e.g. Hatzfeld *et al.* 1997) that the Aegean behaves like a fluid submitted to an extensional boundary condition at its southwestern and southern boundaries due to the low elevations of the ocean seafloor. They argued that the present deformation of the Aegean likely results from differences in gravitational potential energy in the lithosphere. Özeren & Holt (2010) further confirmed that gravitational potential energy differences play an equal part as boundary forces in the dynamics of the Eastern Mediterranean.

As Tirel *et al.* (2004) for the Aegean, we observe a minimum crustal thickness of 20 km at the southernmost end of the profile beneath the Mediterranean coast and the Island of Rhodos where strong extension could be explained by the vicinity of the retreating trench adding tractions to gravitational potential energy differences (Özeren & Holt 2010). However, in contrast to the Aegean Sea, the crust beneath the NAF is not more stretched than the crust of the Menderes Massif which is the eastern equivalent of the Cyclades. Moreover, the Menderes is still undergoing active north–south extension, while the internal strain is weak in the Southern Aegean due to lower gravitational potential energy difference (Floyd *et al.* 2010). The model derived by Tirel *et al.* (2004) for the Aegean thus does not apply in Western Anatolia.

4.2 No detectable intra-crustal structure

A set of laterally coherent north-dipping conversions is detected inside the crust beneath the Northern Menderes Massif (Fig. 5d). Starting from the surface, their polarity is alternatively positive (red), negative (blue) and positive again. The shallowest conversion intersects the surface in the vicinity of the southern bounding fault of the Gediz Graben. We interpret this set of signals as the conversion at the base of the sediments of the graben and its multiples. Yılmaz *et al.* (2000) report that the thickness of the sedimentary infill of the Gediz Graben is more than 3 km, much less than what is observed in the migrated section of Fig. 5(d) ($\sim$10 km). As the migration is achieved with vertically constant *Vp* and *Vp*/*Vs* for the whole crust, the depth estimates are not accurate for shallow structures. More realistic larger values of *Vp*/*Vs* in the shallow crust would move the interfaces to shallower depths. The second conversion at a depth of $\sim$20 km has amplitude and time suggesting that it may be a multiple bouncing within the graben.

To test the accuracy of the crustal model obtained from the CCP analysis and show that the converted energy observed above the crust–mantle boundary may be explained by the shallow structure, we computed a synthetic CCP section from the crustal thicknesses and *Vp*/*Vs* model determined from the receiver-function analysis (Fig. 6). Synthetic RFs are computed for each station using the 1-D velocity models of Table 1 and the reflectivity method. To improve the fit to the observed depth section of Fig. 5, we added a shallow structure to the 1-D velocity model beneath each station (Fig. 6d). However, the thickness and velocity of the shallow layers are poorly known. The thickness of the sediments in the Marmara Sea (3–5 km) is known from the reflection and wide-angle refraction surveys presented in Bécel *et al.* (2009). In the Thrace basin, it is reported that the maximum thickness might exceed 9 km (Görür & Okay 1996). In the Gediz Graben, the thickness of the sediments was reported as at least 3 km from a drilling by the Turkish Petroleum Company (Yılmaz *et al.* 2000). However, the shear wave velocities are unknown. Overall, we constructed the shallow velocity

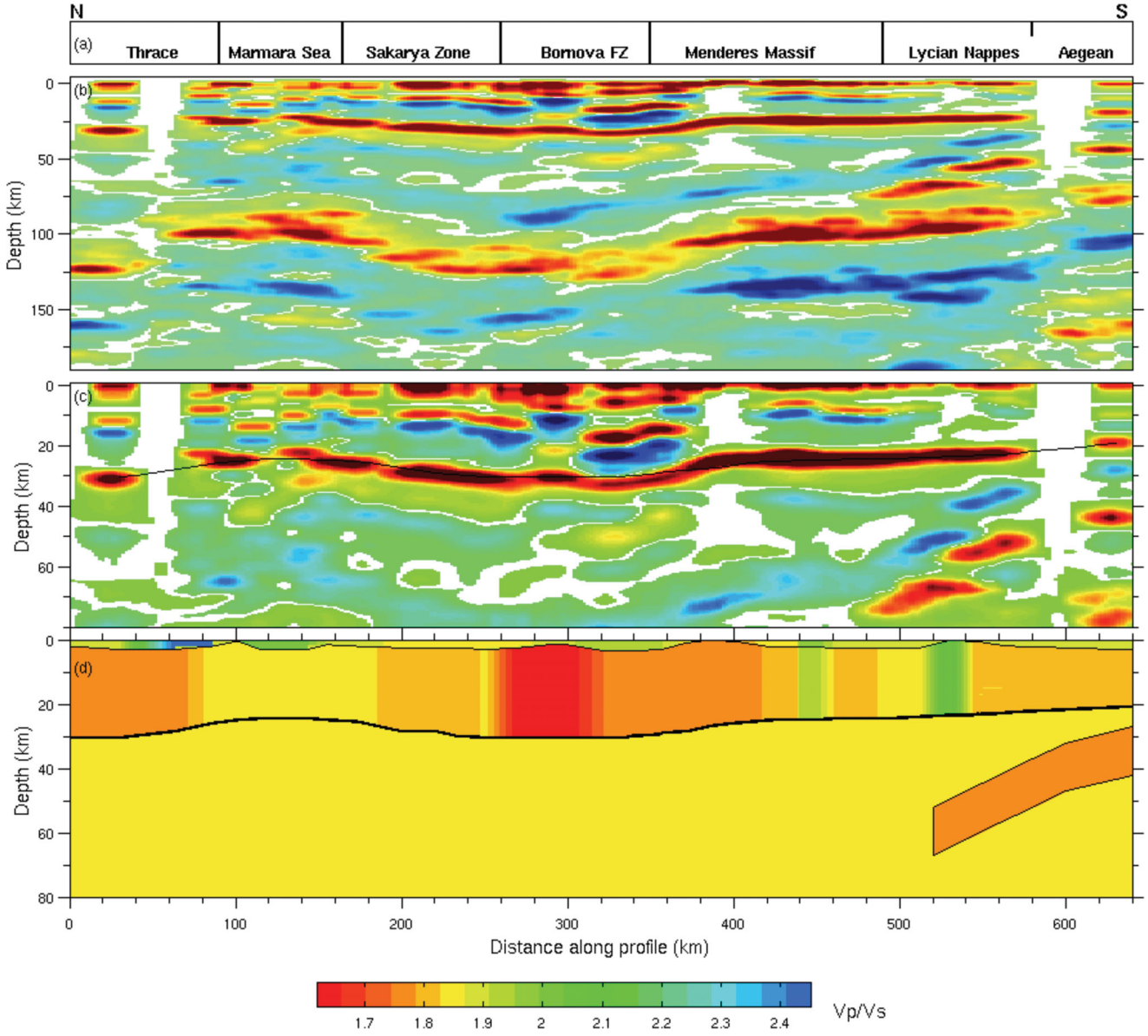

Figure 6. (a) Synthetic-CCP-migrated depth section computed from the crustal thickness and *Vp*/*Vs* models estimated in this study (Table 1). (b) Synthetic-CCP-migrated depth section zoomed for the upper part of model response. (c) Model geometry and *Vp*/*Vs* used for the synthetic CCP depth section. Layer parameters for the subducting plate; $Vp = 6.7$ km/s, $H = 15$ km.

structure shown in Fig. 6(d) by trial and error under the above-cited constraints to have similarity with the CCP image of Fig. 5. The synthetic RFs are computed with the same source-station geometry as the observed data. They are subsequently migrated to depth with the CCP technique using the same *Vp*, *Vp*/*Vs* and crustal thickness models as for the migration of the observed RFs (Table 1).

As a whole, our trial-and-error modelling of the shallow structure successfully leads to a synthetic depth section similar to the observed section (Fig. 6c). Minor differences are observed on the Moho topography beneath the Gediz Graben as the result of using a constant *Vp*/*Vs* ratio for the whole crust and not accounting for the shallow structure in the CCP migration. However, the converted energy observed inside the crust beneath the Gediz Graben in the synthetic section well fits the observations, confirming the hypothesis that the seemingly intra-crustal conversions of Fig. 5d are, in fact, produced by the very shallow structure. Similarly, the apparent upper to mid-crustal signals observed beneath the Thrace basin and the Marmara Sea are conversions at the base of the sediments migrated to incorrect depths by the single-layer velocity model.

As all signals observed at mid- or lower-crustal depths in the migrated section are artefacts, we conclude on the absence of intra-crustal interfaces. We identify none of the main geological structures that could have induced velocity contrasts inside the crust, like the Izmir–Ankara suture or the detachments faults of the Menderes metamorphic core complex. The observed seismically transparent crust may result from pervasive ductile strain in the hot and weak lower crust in response to crustal thickness variations.

4.3 Crustal structure beneath the Sea of Marmara and Menderes Massif

At issue in the debate on the rheology of continental crust, there are the differences in the crustal structure beneath the Sea of

Marmara, which is intersected by the NAF, and the Menderes Massif. The two regions have similar broad-scale Moho topographies with a small uplift of 6–8 km in 150-km distance. The width of the Menderes Moho anomaly is in the order of the width of the massif, whereas the Marmara Moho anomaly is significantly wider than the Sea of Marmara (Fig. 5). This suggests that the broad-scale crustal thinning observed beneath the Marmara is not associated with the late opening of the relatively narrow pull-apart basins of the North Marmara Trough (Şengör *et al.* 2004). Indeed, structural and stratigraphical data show that due to Aegean north–south extension, the Marmara Sea depression first developed as a wide basin extending from the present Thrace Basin in the north to the Bursa-Balıkesir Plateau (Yılmaz *et al.* 2010 and references therein). The extension phase was followed by right-lateral shear when the North-Anatolian Fault zone (NAFZ) reached northwestern Anatolia, leading to the late initiation of the NAF by progressive strain localization (Şengör *et al.* 2004). The early basin thus covered a much larger area than the present limits of the Marmara Sea. We propose that the broad crustal thinning observed beneath the Marmara region originated from this first deformation phase of Aegean N-S extension.

However, Fig. 5 shows that the Moho beneath the Marmara region is not as smooth as beneath the Menderes. The sparser station coverage in the Marmara region might enhance the rough Moho aspect. There is, however, a clear Moho depth change between the two neighbouring stations of the southern shore of the Marmara Sea (Fig. 5d). Moreover, we observe strong variations of the individual RFs with azimuth of the incident wave at stations in the Marmara region, suggesting strong horizontal variations in the crustal structure which are not observed in other parts of the profile. The laterally variable character of the Moho image beneath the Marmara appears in the migrated depth section (Fig. 5d) and in the rapid and strong variations of the reflectivity factor R (Fig. 5e). However, we cannot tell whether this heterogeneity is an intrinsic characteristic of the crust-mantle boundary in the Marmara area or due to scattering in a very heterogeneous crust. This strong crustal heterogeneity might be a consequence of the superposition of N-S extension with right lateral shear in the broad NAFZ and the later NAF. Part of the crustal heterogeneity and/or part of the Moho depth change may be associated with the formation of the North Marmara Trough basins, which are very young structures, probably not older than Late Pliocene (Le Pichon *et al.* 2001; Şengör *et al.* 2004).

The Bouguer gravity high of the Sea of Marmara (Fig. 5a) is too strong to be explained by the limited crustal thinning. Moreover, its large width rules out the hypothesis that it is due to the narrow pull-apart basins of the North Marmara Trough imaged by Bécel *et al.* (2009). The source of the positive gravity anomaly has yet to be looked for at upper- to mid-crustal level, strengthening the idea of a very heterogeneous crust beneath the Marmara as compared to other parts of the profile.

Higher than average Vp/Vs values are observed beneath the Marmara Sea and Thrace Basin (Fig. 5f). In the same area, Love wave group velocities at 20 s (red curve in Fig. 5g) are low, while *Pn* velocities are relatively high (black curve in Fig. 5g), indicating that the high average Vp/Vs is due to low shear wave velocities in the upper crust. They may be attributed to the presence of thick sedimentary basins (∼5 km in the Marmara basins and ∼7 km in the Thrace Basin) and/or to pore fluids in highly fractured rocks along the NAF for the Marmara region.

The crust of the Menderes Massif similarly has high Vp/Vs values of 1.8 to 1.9 indicative of an intermediate composition. The most striking observation is the strong amplitude of the Moho converted phase documented by high (>0.4) and spatially consistent values of R beneath the Southern Menderes Massif (Fig. 5e). As discussed by Nair *et al.* (2006), the R values mostly reflect the sharpness of the Moho that is the width of the crust–mantle transition. The high values of R beneath the Southern Menderes Massif suggest a particularly thin Moho transition zone.

The effect of very large (>1.90) Vp/Vs values on the CCP section was investigated by replacing high values by the regional average (see Fig. S3). This test shows that the very high values of Vp/Vs in the Thrace Basin to the north and the Gökova Gulf to the south are constrained by the continuity of the Moho converted phase.

4.4 Subduction beneath the Mediterranean coast

The amplitude of the Moho converted phase is significantly weaker in the Lycian Nappes to the south of the Menderes Massif as documented by values of R in the range 0.2–0.3. The most striking observation is a strong converted phase of positive polarity at upper mantle depth of 45–60 km. It is located below a negative polarity conversion of similar dip. Although we lack stations between Rhodos Island and the Mediterranean coast of Turkey, we are confident that the top of subducting African lithosphere is imaged as the negative polarity north dipping boundary underlined by a dot-and-dash line in Fig. 5(d). The underlying positive polarity converted phase may correspond to the African Moho. It dips at an angle smaller than 30° from approximately 30 km depth beneath Rhodos Island to ∼50 km beneath station YER0 in the Lycian Nappes where it terminates abruptly. Sodoudi *et al.* (2006) also identified the so-called 'African Moho' in their *P* RFs at station RODO in Rhodos Island, at 46 km depth beneath an 'Aegean Moho' at 25 km. Their depth estimates are larger than ours (30 and 20 km) due to the difference between the Vp/Vs they assumed (1.73) and the one we measured at station ARG (1.85). The synthetic section of Fig. 6 which takes into account the north-dipping subduction compares well with the observations at the southern end of the array both for the polarities and times of the converted phases (compare with Fig. S4). The low values of R observed in the Lycian Nappes may be due to sub-crustal heating above the subduction zone that would reduce the velocity contrast at the Moho. The Vp/Vs ratio reaches 1.95 at stations close to abundant hydrothermal resources and extremely large values (>2) between stations W20 and YER0 (500–540 km) which are located right above the tip of the subducted African lithosphere. Love wave group velocities at 20 s (red curve in Fig. 5g) are low where Vp/Vs is high, indicative of low crustal shear wave velocities consistent with a hot crust. Moreover, *Pn* velocities (black curve in Fig. 5g) are low, in agreement with a hot low-velocity mantle wedge above the subduction zone.

4.5 Structure and seismicity

Fig. 5(d) shows that the seismicity is mostly concentrated within the active fault zones, the NAF, the Izmir–Ankara Suture zone, the Gökova Gulf and the subduction zone. The only departure from the brittle upper crust model is the Gökova Gulf where earthquake foci are observed down to Moho depth. A possible explanation is partially melted lower crust above the subduction zone, as it generates granitic magmas leaving behind dry mafic granulites with more brittle rheology (Maggi *et al.* 2000). The seismicity in the subduction zone is diffuse and not clearly correlated with the interface observed in the depth-migrated section. This may be related to poor depth constraints on hypocentre locations.

5 CONCLUSIONS

A RF analysis of records from the first dense array spanning Western Turkey from north to south confirms that extension has significantly thinned the crust to 25 km beneath the Sea of Marmara and the Menderes Massif and 20 km beneath the Mediterranean coast. The Moho beneath the metamorphic core complexes of the Menderes Massif is locally flat, unaffected by the present-day higher extensional strain rates of the Gediz and Büyük Menderes grabens. The discrepancy between the small-scale changes in geodetic strain rate and rugged surface topography and the flat crust–mantle boundary likely results from viscous flow in a hot lower crust smoothing out the rapid changes in crustal thickness. In contrast to the Basin and Range extensional province, the crust–mantle boundary of Western Anatolia is not flat at regional scale. It displays long-wavelength undulations with depth differences of 6–7 km in 150-km horizontal distance from the two Moho highs of the Marmara and the Menderes to the Moho low beneath the Izmir–Ankara suture zone. The shallowest Moho depth of 20 km is measured at stations on the Mediterranean coast and Rhodos Island. According to the gravity modelling of Tirel *et al.* (2004), the thinnest crust of the Aegean is also observed in its southern part, with 22–23 km in the Cretan Sea. In Western Anatolia like in the Aegean, it is likely that the minimum crustal thickness observed in the southernmost region is explained by the vicinity of the retreating trench adding tractions to gravitational potential energy differences (Özeren & Holt 2010). From the Sea of Marmara to the Menderes, the correlation between the north–south changes of crustal thickness and geodetic strain rate suggests that the crustal thickness is a reliable indicator of the finite strain assuming like Aktuğ *et al.* (2009) that a constant strain rate has been applied in the last 5 Ma to a crust of initially constant thickness equal to the present thickness of the rigid plateau of Central Anatolia.

The width of the Moho uplift in the Marmara region is significantly larger than the horizontal extent of the Sea of Marmara. The basins in the Marmara region which, according to Armijo *et al.* (2002), result from the step-over within the northern branch of the NAF, would therefore be shallow structures with limited influence on the crust–mantle boundary. Moreover, this difference in width suggests that the Marmara basins extend beyond the limits of the Marmara Sea, confirming the hypothesis of Yılmaz *et al.* (2010) that the broad structural depression was induced by Western Anatolia N-S extension predating the initiation of shear along the NAFZ. The heterogeneity of the Marmara crust is evidenced by strong changes of RF waveforms with backazimuth and a strong Bouguer anomaly. The Izmir–Ankara suture and its complex suite of underthrusted and exhumed metamorphic suites of the Tavşanlı and Afyon zones (see e.g. the crustal-scale cross section in van Hinsbergen *et al.* 2010) are surprisingly transparent to seismic waves. Their signature in the lower crust may have been erased by later extension and associated pervasive ductile strain. In the upper crust, our limited spatial resolution and the presence of strong conversions and multiples from the sediment-basement interface may prevent from imaging upper- and mid-crustal interfaces.

At the southern end of the array, the depth section displays signals beneath the Anatolian Moho interpreted as conversions from the subducted African Moho. The trace of the subduction disappears abruptly and unambiguously that is without being blurred by the multiple of the Anatolian Moho, 50 km to the north of the Mediterranean coast. The average crustal *Vp*/*Vs* ratio is very high right above the northernmost tip of the African Moho due to low shear wave velocities indicative of a hot crust. The abrupt termination of the subducted lithosphere confirms the presence of a slab tear beneath southwest Anatolia, as suggested by body wave tomography (Spakman *et al.* 1993) and surface wave tomography (Salaün *et al.* 2012). This slab tear might have allowed the rapid retreat of the Hellenic trench, strengthening the extension in the Aegean and Western Anatolia. It might also have played a role in raising temperature in the Anatolian lithosphere, hence contributing to the mechanically weak character of the lower crust.

ACKNOWLEDGEMENTS

We are grateful to all participants in the field work and database preparation. Reviews by L. Jolivet and an anonymous reviewer helped improving the manuscript. Most figures were created using the Generic Mapping Tools (Wessel & Smith 1998). Instruments for temporary stations were provided by the French national RESIF-SISMOB instrument pool with additions from ISTerre and the Geology Laboratory of ENS Paris. The SIMBAAD project is funded by Agence Nationale de la Recherche (France) under contract ANR-06-BLAN-0317.

REFERENCES

Ateş, A., Kearey, P. & Tufan, S., 1999. New gravity and magnetic anomaly maps of Turkey, *Geophys. J. Int.,* **136,** 499–502.

Aktuğ, B. *et al.*, 2009. Deformation of western Turkey from a combination of permanent and campaign GPS data: limits to block-like behavior, *J. geophys. Res.,* **114,** B10404, doi:10.1029/2008JB006000.

Armijo, R., Meyer, B., Hubert, A. & Barka, A., 1999. Westward propagation of the North Anatolian fault into the northern Aegean: timing and kinematics, *Geology,* **27**(3), 267–270.

Armijo, R., Meyer, B., Navarro, S., King, G. & Barka, A., 2002. Asymmetric slip partitionning in the Marmara Sea pull-apart: a clue to propagation processes of the North Anatolian Fault, *Terra Nova,* **14**(2), 80–84.

Bécel, A. *et al.*, 2009. Moho, crustal architecture and deep deformation under the North Marmara Trough, from the SEISMARMARA Leg 1 offshore–onshore reflection–refraction survey, *Tectonophysics,* **467,** 1–21.

Block, L. & Royden, L.H., 1990. Core complex geometries and regional scale flow in the lower crust, *Tectonics,* **9,** 557–567.

Bozkurt, E. & Oberhänsli, R., 2001. Menderes Massif (Western Turkey): structural, metamorphic and magmatic evolution—a synthesis, *Int. J. Earth Sci.,* **89,** 679–708.

Brun, J-P. & Faccenna, C., 2008. Exhumation of high-pressure rocks driven by slab rollback, *Earth planet. Sci. Lett.,* **272,** 1–7.

Cambaz, M.D. & Karabulut, H., 2010. Love wave group velocity maps of Turkey and surrounding regions, *Geophys. J. Int.,* **181,** 502–520.

Çemen, I., 2010. Extensional tectonics in the Basin and Range, the Aegean, and Western Anatolia: Introduction, *Tectonophysics,* **488,** 1–6.

Christensen, N.I., 1996. Poisson's ratio and crustal seismology, *J. geophys. Res.,* **101**(B2), 3139–3156.

de Boorder, H., Spakman, W., White, S.H. & Wortel, M.J.R., 1998. Late Cenozoic mineralization, orogenic collapse and slab detachment in the European alpine belt, *Earth planet. Sci. Lett.,* **164,** 569–575.

Dewey, J.F. & Şengör, A.M.C., 1979. Aegean and surrounding regions complex multiplate and continuum tectonics in a convergent zone, *Geol. Soc. Am. Bull. I,* **90,** 84–92.

England, P.C. & McKenzie, D.P., 1982. A thin viscous sheet model for continental deformation, *Geophys. J. R. astr. Soc.,* **70,** 295–321.

Faccenna, C. & Becker, T., 2010. Shaping the belts by small-scale convection, *Nature,* **465,** 602–605.

Floyd, M.A. *et al.*, 2010. A new velocity field for Greece: implications for the kinematics and dynamics of the Aegean, *J. geophys. Res.,* **115,** B10403, doi:10.1029/2009JB007040.

Fountain, D.M. & Christensen, N.I., 1989. Composition of the continental crust and upper mantle: a review, in *Geophysical Framework of the Continental United States,* Vol. 172, pp. 711–742, eds Pakiser, L.C. & Mooney, W.D., Geol. Soc. Am. Mem., Boulder, CO.

Gautier, P., Brun, J.-P., Moriceau, R., Sokoutis, D., Martinod, J. & Jolivet, L., 1999. Timing, kinematics and cause of Aegean extension: a scenario based on a comparison with simple analogue experiments, *Tectonophysics,* **315,** 31–72.

Gessner, K., Ring, U., Johnson, C., Hetzel, R., Passchier, C.H. & Güngör, T., 2001. An active bivergent rolling-hinge detachment system: Central Menderes metamorphic core complex in western Turkey, *Geology,* **29**(7), 611–614.

Görür, N. & Okay, A.I., 1996. A fore-arc origin for the Thrace Basin, NW Turkey, *Geol. Rundsch.,* **85,** 662–668.

Gurnis, M., 1990. Bounds on global dynamic topography from Phanerozoic flooding of continental platforms, *Nature,* **344,** 754–766.

Hetenyi, G., 2007. Evolution of deformation of the Himalayan prism: from imaging to modelling, *PhD thesis,* Ecole Normale Superieure, Universite Paris-Sud XI.

Hatzfeld, D., Martinod, J., Bastet, G. & Gautier, P., 1997. An analog experiment for the Aegean to describe the contribution of gravitational potential energy, *J. geophys. Res.,* **102,** 649–659.

Hauser, E. *et al.*, 1987. Crustal structure of eastern Nevada from COCORP deep seismic reflection data, *Bull. geol. Soc. Am.,* **99,** 833–844.

Hubans, F., 2010. Utilisation des corrélations de bruit micro-sismique pour l'analyse des propriétés du champ d'onde et l'imagerie crustale, *PhD thesis,* Grenoble University.

Jackson, J., 2002. Strength of the continental lithosphere: time to abandon the jelly sandwich? *GSA Today,* **12,** 4–10.

Jolivet, L., Faccenna, C. & Piromallo, C., 2009. From mantle to crust: stretching the Mediterranean, *Earth planet. Sci. Lett.,* **285,** 198–209.

Jolivet, L. *et al.*, 2012. Aegean Tectonics: Strain localisation, slab tearing and trench retreat, *Tectonophysics,* doi:10.1016/j.tecto.2012.06.011.

Kiratzi, A. & Louvari, E., 2003. Focal mechanisms of shallow earthquakes in the Aegean Sea and the surrounding lands determined by waveform modeling: a new database, *J. Geodyn.,* **36,** 251–274.

Klemperer, S.L., Hauge, T.A., Hauser, E.C., Oliver, J.E. & Potter, C.J., 1986. The Moho in the northern Basin and Range province, Nevada, along the COCORP 40°N seismic-reflection transect, *Bull. geol. Soc. Am.,* **97,** 603–618.

Langston, C.A., 1977. The effect of planar dipping structure on source and receiver responses for constant ray parameter, *Bull. seism. Soc. Am.,* **67,** 1029–1050.

Le Pichon, X. & Angelier, J., 1979. Hellenic arc and trench system – key to the neotectonic evolution of the eastern Mediterranean area, *Tectonophysics,* **60**(1–2), 1–42.

Le Pichon, X. & Angelier, J., 1981. The Aegean Sea, *Phil. Trans. R. Soc. Lond.,* **300,** 357–372.

Le Pichon, X. *et al.*, 2001. The acti,e Main Marmara Fault, *Earth planet. Sci. Lett.,* **192,** 595–616.

Le Pichon, X. & Kreemer, C., 2010. The miocene to present kinematic evolution of the eastern Mediterranean and Middle East and its implications for dynamics, *Ann. Rev. Earth planet. Sci.,* **38,** 323–351.

Ligorria, J.P. & Ammon, C.J., 1999. Iterative deconvolution and receiver-function estimation, *Bull. seism. Soc. Am.,* **89,** 1395–1400.

Lister, G.S., Banga, G. & Feenstra, A., 1984. Metamorphic core complexes of Cordilleran type in the Cyclades, Aegean Sea, Greece, *Geology,* **12,** 221–225.

Maggi, A., Jackson, J.A., McKenzie, D.P. & Priestley, K., 2000. Earthquake focal depths, effective elastic thickness, and the strength of the continental lithosphere, *Geology,* **28,** 495–498.

Makris, J., 1978. The crust and upper mantle of the Aegean region from deep seismic sounding, *Tectonophysics,* **46,** 269–284.

McClusky, S. *et al.*, 2000. Global Positioning System constraints on plate kinematics and dynamics in the eastern Mediterranean and Caucasus, *J. geophys. Res.,* **105**(B3), 5695–5720.

McKenzie, D., Nimmo, F., Jackson, J.A., Gans, P.B. & Miller, E.L., 2000. Characteristics and consequences of flow in the lower crust, *J. geophys. Res.,* **105,** 11 029–11 046.

Mutlu, A.K. & Karabulut, H., 2011. Anisotropic Pn tomography of Turkey and adjacent regions, *Geophys. J. Int.,* **187,** 1743–1758.

Nair, K.S., Gao, S.G., Liu, K.H. & Silver, P.G., 2006. Southern African crustal evolution and composition: constraints from receiver function studies, *J. geophys. Res.,* **111,** B02304, doi:10.1029/2005JB003802.

Okay, A.I. & Tüysüz, O., 1999. Tethyan Sutures of Northern Turkey, in *The Mediterranean Basins: Tertiary Extension Within the Alpine orogen,* Vol. 156, pp. 475–515, eds. Durand, B., Jolivet, L., Horváth, F. & Séranne, M., Geological Society Spec. Pub, London.

Owens, T.J., Zandt, G. & Taylor, S.R., 1984. Seismic evidence for ancient rift beneath the Cumberland plateau, Tennessee: a detailed analysis of broadband teleseismic P waveforms, *J. geophys. Res.,* **89,** 7783–7795.

Özeren, S. & Holt, W.E., 2010. The dynamics of the eastern Mediterranean and eastern Turkey, *Geophys. J. Int.,* **183,** 1165–1184.

Pe-Piper, G. & Piper, D.J.W., 2006. Unique features of the Cenozoic igneous rocks of Greece, in *Postcollisional Tectonics and Magmatism in the Mediterranean Region and Asia,* Vol. 409, pp. 259–282, eds. Dilek, Y. & Pavlides, S., Geological Society of America, Special Papers.

Reilinger, R. *et al.*, 2006. GPS constraints on continental deformation in the Africa-Arabia-Eurasia continental collision zone and implications for the dynamics of plate interactions, *J. geophys. Res.,* **111,** B05411, doi:10.1029/2005JB004051.

Salaün, G. *et al.*, 2012. High-resolution surface wave tomography of the Aegean-Anatolia region: constraints on upper mantle structure, *Geophys. J. Int.,* **190,** 406–420.

Saunders, P., Priestley, K. & Taymaz, T., 1998. Variation in the crustal structure beneath western Turkey, *Geophys. J. Int.,* **134,** 373–389.

Sodoudi, F. *et al.*, 2006. Lithospheric structure of the Aegean obtained from P and S receiver functions, *J. geophys. Res.,* **111,** B12307, doi:10.1029/2005JB003932.

Spakman, W., van der Lee, S. & van der Hilst, R.D., 1993. Travel-time tomography of the European-Mediterranean mantle down to 1400 km, *Phys. Earth planet. Int.,* **79,** 3–74.

Şengör, A.M.C. & Yılmaz, Y., 1981. Tethyan evolution of Turkey: a plate tectonic approach, *Tectonophysics,* **75,** 181–241.

Şengör, A.M.C., Tüysüz, O., İmren, C., Sakınç, M., Eyidoğan, H., Görür, N., Le Pichon, X. & Rangin, C., 2004. The North Anatolian fault: a new look, *Ann. Rev. Earth planet. Sci.,* **33,** 1–75.

Tapponnier, P., Peltzer, G., Dain, A.Y.L., Armijo, R. & Cobbold, P., 1982. Propagating extrusion tectonics in Asia: new insights from simple experiments with plasticine, *Geology,* **10,** 611–616.

Tirel, C., Gueydan, F., Tiberi, C. & Brun, J.-P., 2004. Aegean crustal thickness inferred from gravity inversion. Geodynamical implications, *Earth planet. Sci. Lett.,* **228,** 267–280.

Tirel, C., Brun, J.-P. & Burov, E., 2008. Dynamics and structural development of metamorphic core complexes, *J. geophys. Res.,* **113,** B04403, doi:10.1029/2005JB003694.

Tseng, T.-L. & Chen, W.-P., 2006. Probing the Southern Indian shield with *P*-wave receiver-function profiles, *Bull. seism. Soc. Am.,* **96,** doi:10.17850/0120050074.

van Hinsbergen, D.J.J., Kaymakçı, N., Spakman, W. & Torsvik, T.H., 2010. Reconciling the geological history of western Turkey with plate circuits and mantle tomography, *Earth planet. Sci. Lett.,* **297,** 674–686.

Yılmaz, Y., Genç, X.C., Gürer, F., Bozcu, M., Yılmaz, K., Karacık, Z., Altunkaynak, X. & Elmas, A., 2000. When did the western Anatolian grabens begin to develop?, in *Tectonics and Magmatism in Turkey and the Surrounding Area,* Vol. 173, pp. 353–384, eds Bozkurt, E., Winchester, J.A. & Piper, J.D.A., Geological Society of London, Special Publication.

Yılmaz, Y., Gökaşan, E. & Erbay, A.Y., 2010. Morphotectonic development of the Marmara region, *Tectonophysics,* **488,** 51–70.

Watts, A.B. & Burov, E.B., 2003. Lithospheric strength and its relationship to the elastic and seismogenic layer thickness, *Tectonophysics,* **213,** 113–131.

Wessel, P. & Smith, W.H.F., 1998. New, improved version of Generic Mapping Tools released, *EOS, Trans. Am. geophys. Un.,* **79,** 579.

Wortel, M.J.R. & Spakman, W., 2000. Subduction and slab detachment in the Mediterranean-Carpathian region, *Science,* **290,** 1910–1917.

Zandt, G. & Ammon, C.J., 1995. Continental Crustal composition constrained by measurements of crustal Poisson's ratio, *Nature,* **374,** 152–154.

Zhu, L.P., 2000. Crustal structure across the San Andreas Fault, southern California from teleseismic converted waves, *Earth planet. Sci. Lett.,* **179,** 183–190.

Zhu, L.P. & Kanamori, H., 2000. Moho depth variation in southern California from teleseismic receiver functions, *J. geophys. Res.,* **105,** 2969–2980.

Zhu, L., Mitchell, B.J., Akyol, N., Çemen, I. & Kekovali, K., 2006. Crustal thickness variations in the Aegean region and its implications for the extension of continental crust, *J. geophys. Res.,* **111,** B01301, doi:10.1029/2005JB003770.

SUPPORTING INFORMATION

Additional Supporting Information may be found in the online version of this article:

Figure S1. (Top) (a) RFs of the broadband station LOD plotted as a function of distance. Traces in every 0.4° are displayed. (b) *H-k* stack of the RFs with estimated *Vp*/*Vs* and crustal thickness for ($w_1 = 0.7$, $w_2 = 0.2$, $w_3 = 0.1$). (Bottom) *H-k* stack of (c) Ps phase, (d) PpPs phase and (e) PsPs phase.

Figure S2. Travel time–distance curves along the profile constructed from earthquakes located less than 10 km on either side of the stations.

Figure S3. Migrated depth sections of Ps mode with different *Vp*/*Vs* models. (a) Large values of *Vp*/*Vs* are replaced with the regional average of 1.8 (blue line); (b) same section as in Fig. 4, using the estimated *Vp*/*Vs* (red dots).

Figure S4. (a) Synthetic CCP migrated depth section computed from the crustal model with no subduction. (b) Synthetic CCP migrated depth section zoomed for the upper part of model response. (c) Model geometry and parameters used for synthetic CCP depth section. (http://gji.oxfordjournals.org//lookup/supp1/doi:10.1093/gji/ggt100/-/DC1)

Please note: Oxford University Press are not responsible for the content or functionality of any supporting materials supplied by the authors. Any queries (other than missing material) should be directed to the corresponding author for the article.